Molecular size matters: ultrafast dye singlet sensitization pathways to bright nanoparticle emission

*Jing Liu[1], Pieter Geiregat[2], Luca Pilia[3], Rik Van Deun[2] and Flavia Artizzu[2]**

Dr. J. Liu
Key laboratory of Luminescent and Real-Time Analytical Chemistry
Institute for Clean Energy and Advanced Materials
Faculty of Materials and Energy
Southwest University
Chongqing 400715, P. R. China

Prof. P. Geiregat, Prof. R. Van Deun, Dr. F. Artizzu
Department of Chemistry
Ghent University
Krijgslaan 281-S3, B-9000, Ghent, Belgium
E-mail: flavia.artizzu@ugent.be

Prof. L. Pilia
Department of Mechanical
Chemical and Materials Engineering
University of Cagliari
Via Marengo 2, 09123, Cagliari, Italy

Dye-sensitized luminescent lanthanide (Ln) based nanoparticles enable broad applications spanning from fluorescent microscopy to biological therapy. However, the limited understanding of the dye→Ln^{3+} sensitization process still leaves ample room for the improvement of its efficiency. In this work, we employ a unique combination of photoluminescence and transient absorption spectroscopy to reveal the hereto hidden dye→Ln^{3+} or dye→Ln_1^{3+}→Ln_2^{3+} energy transfer pathways in the ultrafast time scale. Steady-state and time-resolved data, supported by DFT calculations, demonstrate that Ln^{3+} sensitization is realized directly from the singlet excited state of dye molecules and is strictly regulated by a distance dependent regime overcoming the role of the donor-acceptor spectral overlap. We show that exceptionally high efficiency is achieved by judiciously selecting small-sized dye molecules with localized molecular orbitals sitting close (<0.5 nm) to the nanoparticle surface. This new understanding will enable a rational design of dye-sensitized Ln nanoparticles

allowing for a dramatic improvement of the emission efficiency in a variety of nanomaterials for light conversion.

1. Introduction

Dye-sensitized lanthanide (Ln)-based luminescent nanoparticles attract great interest in many research and application fields,[1-3] like photodynamic therapy,[4,5] biological imaging,[4,6] biosensors,[7] displays,[8] anticounterfeiting[9,10] and solar cells,[11,12] thanks to the narrow and long-lived Ln-centered emission, originating from parity-forbidden f-f transitions. In these systems, organic dye molecules act as sensitizers, efficiently harvesting light and transferring the absorbed energy to the Ln ions (Ln^{3+}) (antenna effect) resulting in a strong luminescence enhancement compared to the direct excitation of bare nanoparticles.[13,14] This mechanism of energy transfer (ET) can in principle occur either from the singlet S_1 (SET) or through activated triplet T_1 (TET) excited states of the organic donor dye.[15] The latter event can be triggered by Ln^{3+} ions, which can promote the spin-forbidden intersystem crossing (ISC) from singlet to triplet excited states of nearby organic molecules thanks to strong spin-orbit coupling ('heavy atom effect').[16-21]

Recently, Garfield et al. reported that Gd^{3+} doping in dye sensitized nanoparticles results in an increase in the emission intensity.[22] This finding was attributed to the enrichment of the dye triplet population as a consequence of the heavy atom effect exerted by the optically-silent Gd^{3+}, in turn leading to enhanced sensitization. The activation of a triplet state, which is significantly longer-lived than excited singlets as a consequence of the spin selection rule, was deducted through steady-state time-gated photoluminescence (PL) spectroscopy and triplet quenching experiments, but, regrettably, time-resolved studies allowing for a direct TET signature are absent. The role of the ET mechanisms at the organic-inorganic interface in the emission efficiency of dye-sensitized Ln-based nanoparticles has been very recently highlighted by Wen et al.[19] However, despite the intensive research, until now, no direct evidence of the evolution of the photocycle has been provided and the understanding of the actual key factors governing

the efficiency of the dye to lanthanide sensitization remains largely speculative. Since the two possible ET routes from high-energy singlet or lower-energy triplet are associated to different kinetics, energy levels and spin states, they will be naturally subjected to competitive energy loss channels of different nature (i.e. fluorescence, phosphorescence, energy back transfer, thermal/vibrational deactivation, triplet annihilation).[23,24]

Therefore, disentangling the substeps in the dye→Ln^{3+} sensitization pathway is crucial to establish the parameters to realize a highly efficient photocycle. Conventional PL studies are limited in providing the necessary information, and must be complemented by more advanced transient absorption (TA) spectroscopy investigation. In fact, while steady-state and time-resolved PL only deliver information on bright (radiative) states, on a time scale typically in the range of several ns, TA spectroscopy allows monitoring the temporal evolution of the absorption of transient excited states,[25] which can stem from both bright and dark (non-radiative) channels, on a much faster time scale down to few ps. Thanks to a unique combination of indirect (PL) and direct (TA) evidence, we unravel the dynamics and the intermediate steps of the dye→Ln^{3+} ET mechanism and reveal, with the support of Density Functional Theory (DFT) calculations and the implementation of the Forster's model of resonance ET,[26] the key factors allowing for exceptional near-unity sensitization efficiencies.

2. Results and Discussion

Figure 1a shows in detail the different steps of the energy flow from the sensitizer to the Ln^{3+}. First, the dye is photoexcited from the ground (S_0) to an excited singlet state (S_n), after which it relaxes to the lowest excited singlet state (S_1) through nonradiative internal conversion (IC); S_1 can then directly photoexcite the Ln^{3+} through nonradiative ET, or relax to a lower triplet state (T_1) through ISC, and then feed the Ln^{3+} upper levels. In a remote sensitization configuration, with no direct bonding between the donor dye and the accepting Ln^{3+},[26] the

efficiency of the Ln^{3+} sensitization routes is governed by the 6th power of the inverse of the donor-acceptor distance (R), the spectral overlap integral (J) of the Ln^{3+} absorption and the dye emission, and the dye donor decay rate ($\kappa=1/\tau$, where τ is the lifetime). Since S_1 and T_1 correspond to different spectral ranges and lifetimes, this implies that the nature of the donor feeding state crucially affects the dye→Ln^{3+} sensitization efficiency and a faster SET would be in principle more beneficial that TET.

To uncover the hidden ET pathways and identify the role of S_1 and T_1 in the photocycle, we constructed Ln^{3+} doped core/shell nanoparticles (Fig. S1) embedded in a CaF_2 matrix, as ideal blank support solely constituted by lightweight atoms. This allowed to tune the "heavy atom effect" through the controlled introduction of Gd^{3+}, potentially able to trigger triplet population of a nearby molecule, but unable to receive energy from the dye donor due to its high energy upper level configuration. Nd^{3+} and Yb^{3+} were selected as the emitters since their low-lying emissive levels can allow ET from both S_1 and lower energy T_1 of the dyes in a wide spectral range. Nd^{3+}, which has several absorption lines in the visible (Vis) range, is also an effective sensitizer towards the 1 μm single-line absorber Yb^{3+}, and can work as "energy bridge" between the dye molecules and Yb^{3+} (Fig. 1b).[27] Yb^{3+} is in turn the most commonly used Ln to achieve light upconversion and downconversion besides optical amplification in the NIR.[28] To achieve a full picture of the dye-to-Ln sensitization mechanism in nanoparticles, we selected three dye molecules, namely Coumarin, fluorescein isothiocyanate (FITC), and IR806, enabling a wide emission output from the blue to the near-infrared (NIR) range (Fig. 1c and Fig. S2-4). Fig. 1c highlights the overlap areas of Nd^{3+} and Yb^{3+} absorption with Coumarin, FITC and IR806 fluorescence.

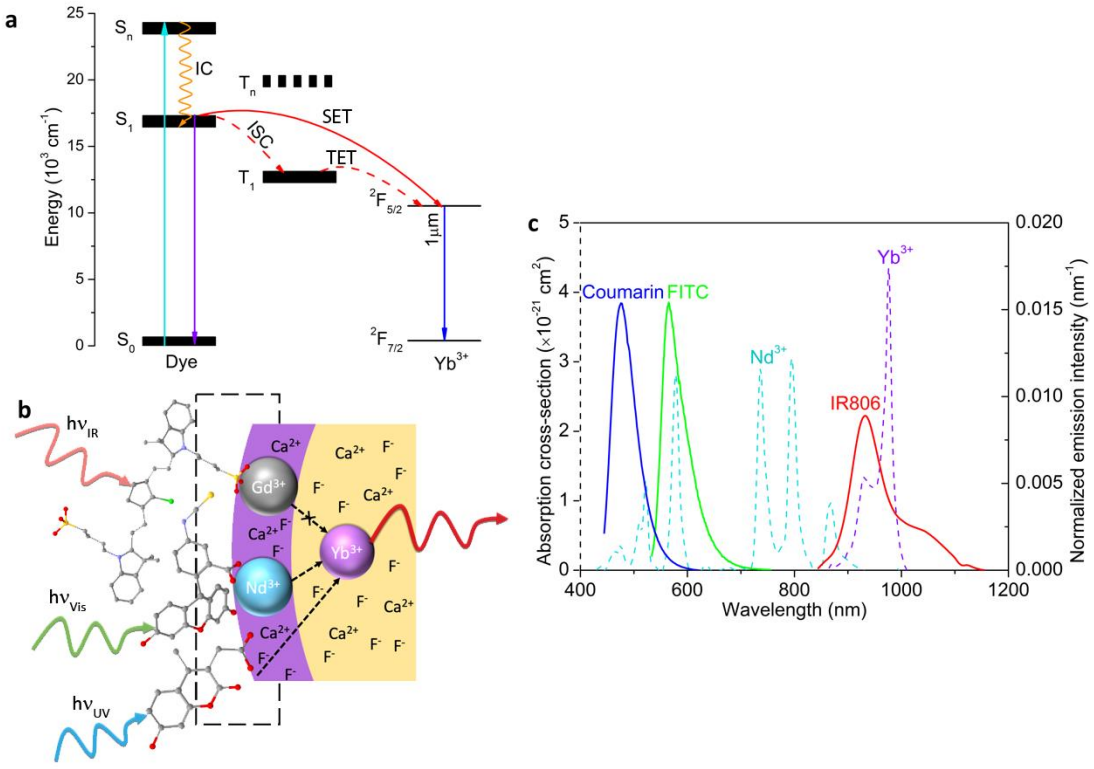

Figure 1. a) Jablonski diagram of possible ET pathways, here shown for Yb^{3+}. b) Scheme of dye sensitized Ln^{3+} based nanoparticles and ET routes. c) Spectral overlap of Ln^{3+} absorption (dashed lines) and dyes fluorescence (solid lines).

To gain first evidence on whether the triplet state is activated, we utilized steady-state and time-resolved PL to investigate the evolution of the dye fluorescence decay ($S_1 \rightarrow S_0$). CaF_2@dye samples are taken as the actual references for the dye emission to account for possible coordination effects and intermolecular interactions.

Figures 2a,c shows that Gd^{3+} doping (30% concentration) does not significantly affect neither the luminescence intensity nor the emission lifetime of the dyes, suggesting that no alternative channel of singlet decay through the population of a triplet level is relevantly triggered even in the presence of the heavy Gd^{3+}.[29-31] Compared to the Gd^{3+}-doped samples, the luminescence intensity and lifetime of the dyes decrease in all other Ln^{3+}-doped systems, due to the competitive depopulation of the excited states by non-radiative ET to the optically active Nd^{3+} and Yb^{3+}. Furthermore, no significant change of Yb^{3+} NIR emission (Fig. 2b and Fig. S9) was

observed in a Gd^{3+}-doped shell/Yb^{3+}-doped core control sample with respect to Yb^{3+} singly-doped nanoparticles. It is also important to note that the Ln^{3+} instant (sub-ns) signal rising in the NIR rules out a feeding route through a long-lived state such as a triplet state (Fig. S9-10).

On the other hand, the dye fluorescence ($S_1 \rightarrow S_0$) decay dynamics is clearly sensitive to the nature of the optically-active Nd^{3+} or Yb^{3+} ions likely as a result of the different spectral overlap (Fig. 1c). Overall, retrieved time constants Table S1) suggest that dye sensitized Nd^{3+}-doped shell/Yb^{3+}-doped core samples always provide the most efficient dye$\rightarrow Ln^{3+}$ ET. This effect is especially remarkable for FITC whose residual emission intensity is almost completely quenched (Fig. 2a). In the case of Coumarin and FITC, this finding stems from the activation of an ultra-efficient dye$\rightarrow$Nd$\rightarrow$Yb channel[27] speeding up the overall dynamics and boosting the Yb^{3+} emission intensity (Fig. 2b and Fig. S9-10). The sensitization efficiencies estimated from temporal data (Table S3)[32,33] remarkably increase from ~75% to ~90% and ~7% to ~36% upon coupling Nd^{3+} to FITC and Coumarin, respectively, in excellent agreement with the trends of the spectral overlap integral $J(S_1 \rightarrow S_0)$ with the dye fluorescent emission (Figure 1c and Table S5), thus strengthening the hypothesis of SET as sensitization pathway without triplet activation. On the other hand, only a relatively limited and constant quenching of the IR806 dye fluorescence is found for the three Nd^{3+}, Yb^{3+} and Nd^{3+}/Yb^{3+} doped particles, with very similar values of ET efficiencies around ~25%. Since the dye fluorescent emission is highly resonant with Yb^{3+} absorption and only partially with Nd^{3+}, this observation points out that $J(S_1 \rightarrow S_0)$ is surprisingly not the dominating factor in Ln^{3+} sensitization in this case, in contrast with the observations made for FITC and Coumarin. The anomalous behavior of the IR806 dye points out the necessity for a more direct and incontrovertible evidence of S_1 as the Ln^{3+} feeding state to ultimately identify the role of the resonance condition (J) over molecular factors affecting the donor-acceptor separation (R), on the efficiency of the photocycle On the other hand, only a relatively limited and constant quenching of the IR806 dye fluorescence is found for the three Nd^{3+}, Yb^{3+} and Nd^{3+}/Yb^{3+} doped particles, with very similar values of ET efficiencies around

~25%. Since the dye fluorescent emission is highly resonant with Yb^{3+} absorption and only partially with Nd^{3+}, this observation points out that $J(S_1 \rightarrow S_0)$ is surprisingly not the dominating factor in Ln^{3+} sensitization in this case, in contrast with the observations made for FITC and Coumarin. The anomalous behavior of the IR806 dye points out the necessity for a more direct and incontrovertible evidence of S_1 as the Ln^{3+} feeding state to ultimately identify the role of *J* over molecular factors affecting the donor-acceptor separation (R), on the efficiency of the photocycle.

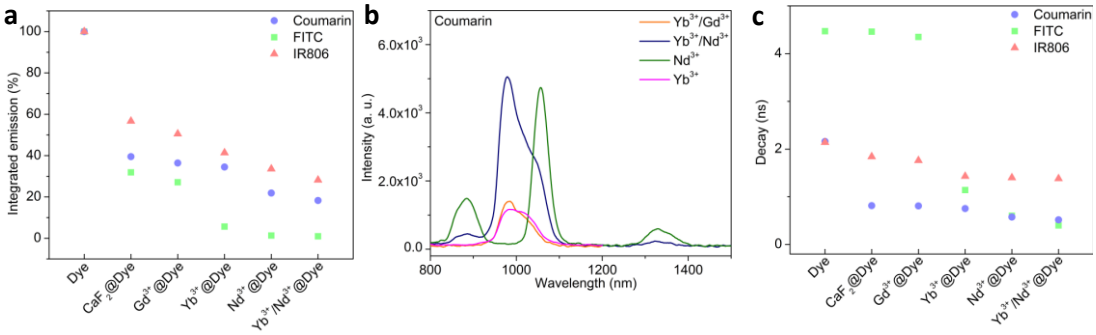

Figure 2. a) Relative change of the dye emission integrated intensity in the free form (FITC, Coumarin and IR806), and bound to CaF_2, CaF_2:Gd^{3+}, CaF_2:Yb^{3+}/CaF_2, CaF_2/CaF_2:Nd^{3+}, CaF_2:Yb^{3+}/CaF_2:Nd^{3+}. b) NIR emission of Ln^{3+} excited Coumarin sensitized CaF_2:Yb^{3+}/CaF_2, CaF_2/CaF_2:Nd^{3+}, CaF_2:Yb^{3+}/CaF_2:Nd^{3+} and CaF_2:Yb^{3+}/CaF_2:Gd^{3+}. Efficient $Nd^{3+} \rightarrow Yb^{3+}$ ET results in an intensity decrease of the Nd^{3+} emission peaks after Yb^{3+} is doped into the core, whereas Yb^{3+} emission at 979 nm is significantly enhanced. c) Relative change in emission lifetimes of the dyes as free molecules (FITC, Coumarin and IR806), and bound to CaF_2, CaF_2:Gd^{3+}, CaF_2:Yb^{3+}/CaF_2, CaF_2/CaF_2:Nd^{3+}, CaF_2:Yb^{3+}/CaF_2:Nd^{3+} nanoparticles.

In light of the above considerations, TA spectroscopy has been used as an effective method to track down the excited-state dynamics of the dye molecules.[30,31,34-37] The dyes were optically pumped in their lowest absorption band (S_1-S_0) and the evolution of their excited states was probed by measuring the change in absorbance (ΔA) across the ultraviolet

(UV) to NIR range. Figures 3a,d,g present the wavelength-time two-dimensional (2D) plots of FITC, Coumarin and IR806 bound to $CaF_2:Yb^{3+}/CaF_2:Nd^{3+}$ while the corresponding data for the remaining samples and a detailed discussion are reported in Supporting Information.

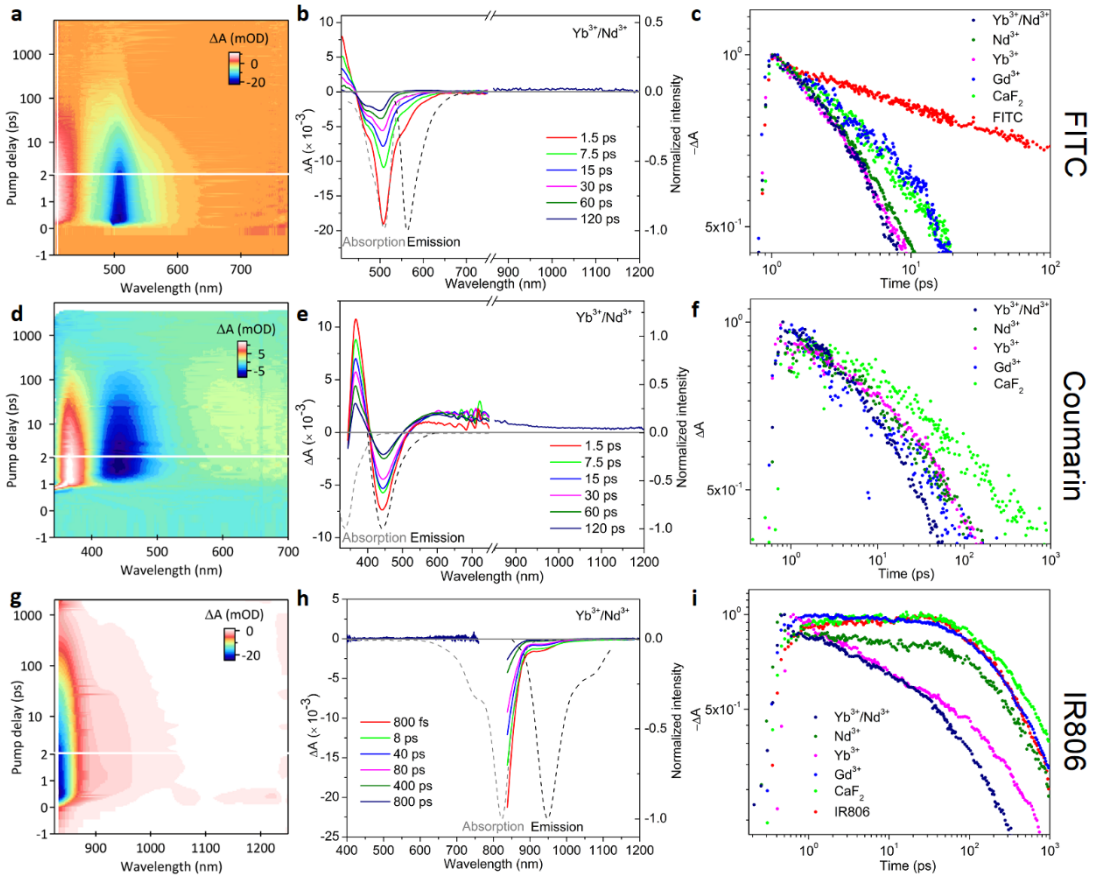

Figure 3. 2D TA (ΔA) map of (a) FITC, (d) Coumarin and (g) IR806 bound to $CaF_2:Yb^{3+}/CaF_2:Nd^{3+}$ in chloroform as a function of wavelength and time, upon photoexcitation at (a) 500 nm, (d) 330 nm, (g) 800 nm. Representative selection of TA spectra of (b) FITC (e) Coumarin and (h) IR806 bound to $CaF_2:Yb^{3+}/CaF_2:Nd^{3+}$ in chloroform at different time delays. The black and grey dash curves show the inverted PL spectrum and ground-state absorption spectrum, respectively. Selected kinetics of (c) FITC, (f) Coumarin and (i) IR806, in the free form and bound to CaF_2, $CaF_2:Gd^{3+}$, $CaF_2:Yb^{3+}/CaF_2$, $CaF_2/CaF_2:Nd^{3+}$, $CaF_2:Yb^{3+}/CaF_2:Nd^{3+}$ nanoparticles probed at (c) 550 nm (SE), (f) 378 nm

(GSB), (i) 840 nm (GSB). Data for the free Coumarin are not available due to strong photobleaching of the molecule during the experiment. Signal was acquired as the absorption A_t at a delay time t of the probe pulse with respect to the excitation pump corrected for the absorption A_0 at a delay t=0, so that $\Delta A = A_t - A_0$.[36]

The three dyes coupled with $CaF_2:Yb^{3+}/CaF_2:Nd^{3+}$ present similar TA features, with strong negative signals attributable to ground-state bleaching (GSB), and stimulated emission (SE) related to the dye S_1 singlet state. These attributions are in agreement with the steady-state absorption and emission shown in Figures 3b,e,h which also report a selection of TA spectra at different time delays. FITC and Coumarin derivatives also display positive signals due to excited state absorption (ESA) to higher energy states. The spectral evolution of the dye excited states after initial pumping to the first excited singlet S_1 level basically follows the same trend for all the three archetypical dyes. Signal build-up develops within 1 ps after optical pumping and subsequently decays with no significant spectral changes suggesting no modifications in the electronic configuration of the dye in the investigated temporal window (up to 6 ns). Hence, no spectral signature of a T_1 state is evidenced.

Fig. 3c,f,i shows the kinetic traces of the TA response of FITC, Coumarin and IR806 dyes. From the instant rising within the probe pulse it can be inferred that these signals correspond to the dynamics of the first excited singlet state S_1, which is observed throughout the probed spectral range. In all hybrid systems, data are best fitted with a double-exponential function, evidencing two major components on a fast (~100 ps) and a slow (> 1 ns) time scale beyond the investigated temporal window. This latter component is

consistent with the observed PL decay data of the dyes fluorescent emission in the few ns range (Fig. 2c and Table S1). Moreover, its relative contribution to the entire TA signal is in agreement with the relative variation of the residual steady-state dye emission intensities in Fig. 2a. Clearly, TA spectroscopy uncovers an ultra-fast excited state dynamics which remains hidden in time-resolved PL studies. Nonetheless, the two observed dynamics in the short and long-time scale evidence a similar general trend on going from the free dye to the control sample $CaF_2:Gd^{3+}$@dye, where the dye→Ln^{3+} ET is suppressed, to the systems containing the photosensitized Yb^{3+} and Nd^{3+}. Observed TA decay traces within a short time scale in Figures 3c,f,i further corroborate the idea that the ET is not mediated by the heavy atom effect, particularly from the comparison of the samples CaF_2@dye and $CaF_2:Gd^{3+}$@dye which does not denote an obvious change in the decay times.[30,31] Interestingly, from the analysis of the decay dynamics in Figures 3c,f,i it can be evidenced that the ET processes to Nd^{3+} and Yb^{3+} occurring on the short time scale are significantly enhanced with respect to that observed in the PL temporal scale. The fast component of the signal for FITC and Coumarin coupled to undoped CaF_2 particles describes time constants that are in the 200-300 ps range and are shortened down to few ps (~11-12 ps) and tens of ps (~80-130 ps) respectively in the presence of the Ln^{3+} acceptors (Supplementary Table 2). It is particularly worth noting that the signal for the Nd^{3+}-containing samples sensitized through FITC is entirely is the ultra-fast sub-100 ps range, in agreement with the negligible residual dye PL emission observed (Figure 2a), suggesting nearly unitary sensitization efficiencies. Nonetheless, as evidenced by the trends in Figures 3c,f, differences in the dynamics of ET

towards Yb^{3+} and Nd^{3+} in the ultra-fast regime are less pronounced than those detected with time-resolved PL spectroscopy.

On the other hand, in the case of the IR806 dye (Figure 3i), a dramatic shortening of the decay times dropping from ~200 to ~40-50 ps is observed for the Yb^{3+}-doped samples yielding an approximate 80% ET efficiency in contrast to the ~25% estimations made with time-resolved PL. Moreover, opposite to the trend in FITC and Coumarin-based systems, the short time scale dynamics of the IR806 dye reveals a much more significant deviation between the decay behavior in Yb^{3+} and Nd^{3+}-doped particles. We can conclude that the dynamics of the IR806 dye in the ultrafast regime confirms the evolution of the photocycle through SET and highlights that additional key factors, beyond the nature of the intermediate state, have significant impact in governing the photocycle and could explain the anomalous behavior observed for this dye in the longer temporal scale.

The double-component dynamics of the dye S_1 state decay is consistent with the existence of two populations of dye molecules in the surroundings of the particle arranged in a double-sphere model configuration as depicted in **Figure 4**a. Molecules directly anchored on the surface of the particle (1st sphere) would transfer energy over a short range on an ultra-fast time scale whereas long range sensitization occurring over longer times would be established from dyes held in the proximity of the particle possibly by intermolecular interactions (2nd sphere).

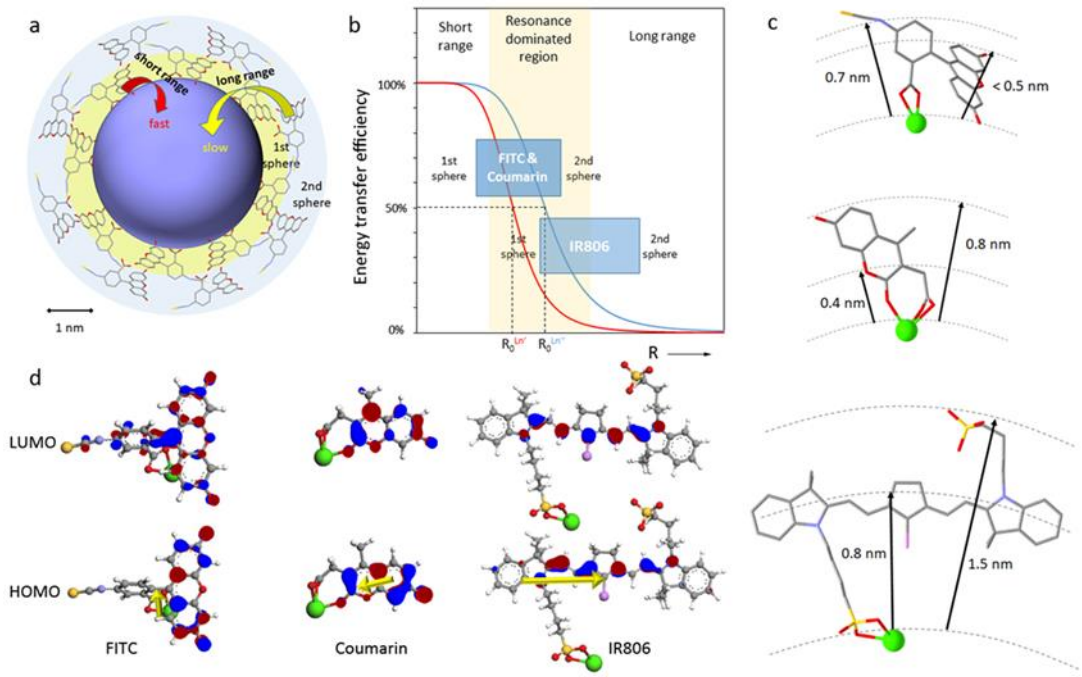

Figure 4. a) Double-sphere model configuration for the dye-sensitized nanoparticles. b) Model of distance-dependent ET according to the Forster's theory for two Ln^{3+} acceptors with different resonance with the dye emission ($J_{Ln''} > J_{Ln'}$). c) Optimized geometry for FITC, Coumarin and IR806 coordinated to Ca^{2+} (green). d) Frontier MOs for FITC, Coumarin and IR806 coordinated to Ca^{2+}. The yellow arrows represent the time-dependent DFT calculated S_1-S_0 transition dipole moment.

We can then interpret the observed trends of the dyes decay dynamics in the framework of the Förster's theory through distance-dependent dipolar coupling from the dye donor in the excited S_1 state to the Ln^{3+} acceptors embedded into the nanoparticle.[38,39] According to the model (see Supporting Information), the ET efficiency varies with the sixth power of R ($\eta \propto R^{-6}$) with a sigmoidal trend where an abrupt drop is comprised between two plateaus. The position of the drop is determined by the magnitude of the overlap integral J_{Ln} between the donor emission and the Ln^{3+} absorption bands (with $J_{Nd} > J_{Yb}$

for FITC and Coumarin and $J_{Yb} > J_{Nd}$ for IR806, Figure 1c).[40,41] J_{Ln} in turn defines the Förster's critical radius R_0, at which $\eta = 0.5$ ($R_0 \propto J_{Ln}$), as depicted in Fig. 4b. When comparing two curves associated to different J_{Ln} values, it is possible to identify three sequential regions of space, the two limits corresponding to 'short-range' and 'long-range' ET where the efficiency of the process is close to unity or approaches zero, respectively. The third region at intermediate distances determines a dramatic change in η for small variations of R according to the overlap integral (J_{Ln}). On the basis of these considerations, the decrease in the gap of the ET efficiency from FITC or Coumarin to Nd^{3+} and Yb^{3+} on going from '2nd sphere' molecules (decaying in the ns time-scale) to '1st sphere' dyes (associated with a ultra-fast dynamics) is consistent with a shift from the 'resonance dominated' towards the 'short range' donor-acceptor ET region in Fig. 4b. On the contrary, the remarkable increase in η for the IR806 to Yb^{3+} ET in the ultra-fast dynamics regime, may be related to a population of 1st sphere dyes comprised in the 'resonance dominated region' in contrast to 2nd sphere dyes at 'long-range' ET distances (Fig. 4b). Although the quantitative determination of overlap integrals can be subjected to errors, R_0 values in the range 0.5-1.1 nm are expected depending on the resonance of the different dyes fluorescence with Nd^{3+} and Yb^{3+} ($J_{Nd/Yb}(S_1 \rightarrow S_0)$, Table S5). As can be seen in Fig. 4c, which reports the DFT-calculated optimized geometries of the dyes upon coordination to a Ca^{2+} ion, these short distances are comparable to the size of the dye molecules. In the electric dipolar coupling ET model, the critical donor-acceptor separation is actually determined by the localization of the transition dipole moment of the dye donor between the first excited state and the ground state. Fig. 4d illustrates the DFT-calculated frontier molecular orbitals (MOs) for

the three investigated dyes which provide a reliable representation of the variation of the molecular electronic distribution and dipole moment accompanying the lowest energy transition S_1-S_0 (Supplementary Table 6). As evidenced by Fig. 4c, the MOs are highly localized on specific portions of the molecules and lie at different distances from the surface of the nanoparticle in the three cases. The shortest separation is realized for FITC which adopts a bent geometry where the electron density of the ground and excited states, and hence the transition dipole moment, is comprised within a distance shorter than 0.5 nm from the surface of the nanoparticle, lying well below the estimated Förster's radius (~0.75 nm, Supplementary Table 5) for outer-shell Nd^{3+} ions. This accounts for the high efficiencies observed for the 1st sphere ET mechanism, while the small molecular size and the opportunity to establish supramolecular interactions through aromatic rings may explain the still favorable conditions of short R for effective 2nd sphere sensitization, according to the above described model depicted in Fig. 4b. This allows for the achievement of an exceptionally high sensitization quantum yield close to unity. Similar considerations can be made for the Coumarin dye, as evidenced in Fig. 4c,d, where the ET efficiency to the Ln is in this case limited by the poor resonance realized through the dye S_1 state (Fig. 1c) implying short R_0 values (< 0.5 nm). On the other hand, the molecular geometry of IR806 confines the highly localized excited and ground state electron density at a distance ~0.8 nm from the surface of the nanoparticles for the directly anchored dyes and significantly further away in the case of 2nd sphere dyes in view of the steric hindrance of the molecule (Fig. S15). These observations, combined with the analysis of the dye decay dynamics and the estimation of the Förster's critical radii (Table S5), support the hypothesis described in Fig.

4b where 2nd sphere dyes lie in a region of 'long-range' ET and bonded molecules in the 'resonance-dominated' one.

These considerations finally shed light on two equally crucial factors governing the efficiency of the dye→Ln^{3+} sensitization in hybrid nanoparticles, namely, the resonance condition of the acceptor with the dye S_1 state $J(S_1 \rightarrow S_0)$ as well as the dye molecular size and geometry, which determines the actual donor-acceptor distance R. At sub-0.5 nm R values, the conditions for unitary sensitization efficiency are established through both dipolar Förster and possible electron exchange Dexter[42] mechanisms.

3. Conclusions

In summary, we have demonstrated that in dye-sensitized Ln-based nanoparticles photosensitization occurs through direct energy transfer from the dye singlet excited states to the Ln^{3+} emitter, without triplet activation, by means of a unique combination of PL and TA spectroscopy. Analysis of the dye excited state decay dynamics in the ultrafast picosecond and the nanosecond timescale, points out the existence of two populations of dyes which can be associated with a 'double-sphere' model consisting of molecules directly anchored to the surface of the nanoparticle and indirectly interacting in the outer sphere through supramolecular noncovalent bonding, transferring energy to the Ln^{3+} in different regimes. DFT calculations, combined with the Förster's energy transfer model, show that the dye→Ln^{3+} energy transfer is crucially regulated by donor-acceptor distances beyond the overlap integral between the Ln^{3+} absorption and the dye fluorescence. In this context, it is also shown that it is possible to achieve near-unity sensitization quantum yields by carefully selecting small-sized dye molecules with suitable excited singlet energy and localized

molecular orbitals close (<0.5 nm) to the surface of the nanoparticle. These findings shed light on the hidden factors governing the photocycle in dye-sensitized lanthanide luminescent nanoparticles providing the guidelines for a rational design of materials for optical amplification and light upconversion/downconversion, thus paving the way for highly efficient solar energy converters or biological applications.

4. Experimental Section

Synthesis of CaF_2:30%Ln^{3+} Core Nanoparticles: The CaF_2 nanoparticles were obtained by a thermal decomposition method.[27,43] To obtain core nanoparticles, 1.0 mmol CaF_2:Yb^{3+}, 0.7 mmol $Ca(CF_3COO)_2$ and 0.3 mmol $Yb(CF_3COO)_3$ oleate-amine solution were mixed in a 50 mL three-neck round-bottom flask. The resulting mixture was degassed under vacuum to remove water and oxygen at 120 ˚C for 40 min and then heated to 310 ˚C for 20 min under nitrogen flow with constant stirring. The obtained core nanoparticles were centrifuged and washed by addition of acetone several times, finally redispersed in cyclohexane.

Synthesis of CaF_2:30%Ln^{3+}/CaF_2 Core/Shell Nanoparticles: CaF_2:Yb^{3+}/CaF_2 core-only nanoparticles were first synthesized as described above. After reaction at 310 ˚C for 20 min, 1 mmol of $Ca(CF_3COO)_2$ precursors were injected into the flask and the mixture was maintained under stirring at 310 ˚C for 15 min. The after-treatment was the same as described for the core-only nanoparticles.

Synthesis of CaF_2:30%Ln^{3+}/CaF_2:30%Ln^{3+} Core/Shell Nanoparticles: CaF_2:Yb^{3+}/CaF_2:Nd^{3+} were obtained by a two-step procedure in which core-only nanoparticles were first synthesized as described above. As a second step, 0.7 mmol of $Ca(CF_3COO)_2$ and 0.3 mmol of $Nd(CF_3COO)_3$ precursors were then injected into the flask and the resulting mixture was maintained under stirring at 310 ˚C for 15 min. The after-treatment was the same as described for the core-only nanoparticles.

Dye modification of Core/Shell Nanoparticles: To obtain dye-decorated nanoparticles, core/shell nanoparticles in chloroform (12 mg/mL) were mixed with dye molecules in chloroform (0.3 mg/mL). The mixture was stirred with heating at 45 ˚C for 16 h. The final solution was washed with acetonitrile and redispersed in chloroform.

Characterization: TEM images were collected using JEOL JEM-2200FS transmission electron microscope operated at 200 kV. UV-vis absorption spectra were obtained with a double beam Perkin Elmer Lambda 900 UV/Visible/NIR spectrometer in transmission mode. Time resolved and steady-state photoluminescence spectroscopy was performed on clear suspensions of the samples in $CHCl_3$, appropriately deaerated by bubbling Ar for 20 minutes. The photoluminescence spectra were recorded on an Edinburgh FLSP 920 UV-vis-NIR spectrofluorimeter with a 450 W xenon lamp as the steady state excitation source and an incident average power of 2 mW/cm^2 in the whole excitation range. For quantitative comparison, all steady-state data have been appropriately normalized for the content of the lanthanide ions and for the absorbed power at excitation wavelength (within series of dye-grafted and dye-free molecules), as determined through absorption spectroscopy. The luminescence emission spectra presented in this paper have been corrected by the setup program for detector sensitivity. Luminescence decay curves in the μs temporal range were measured with a pulsed Xe lamp (100Hz repetition rate, 60W power), whereas time-resolved studies of dye emission in the ns region were performed with a Fianium Supercontinuum white light laser.

Transient Absorption Measurements: Samples were photo-excited using 100 femtosecond pulses (1 kHz) at varying wavelengths, created from an 800 nm Ti:S laser (Spitfire Ace, Spectraphysics) through frequency mixing in a TOPAS optical parametric amplifier (Light Conversion). Broadband probe pulses were generated in a CaF_2 (350-700 nm) and YAG crystals (850 - 1300 nm) using the 800 nm as a seed. The probe was delayed using a delay stage with maximum delay of up to 3.3 ns (Newport TAS). Noise levels of 0.1 mOD (RMS) are obtained

by averaging over 5000 shots per time delay. Using 2 mm path length cuvettes, the samples were stirred during pump-probe measurements to avoid effects of photo-charging and sample degradation. Beam area and shape were evaluated using a Thorlabs CCD Beam profiler.

DFT calculations: Ground-state electronic structure calculations of CaFITC, CaCoumarin and CaIR806 were performed at Density Functional Theory (DFT)[44] level employing the GAUSSIAN 16[45] software package. The functionals used throughout this study were B3LYP[46,47]. The ground state geometries were obtained in the gas phase by full geometry optimization without any symmetry constrain. The basis set employed for all atoms was the valence triple-zeta 6-311+G(d,p).[48,49] All structures were input using ArgusLab 4.0.[50] The effects of solvation on the complexes were took into account using the Polarizable Continuum Model (PCM); the ground state geometries were optimized in a $CHCl_3$ simulated electric field starting from the gas phase optimized geometry. The optimized molecular structures and the orbital isosurfaces were visualized using ArgusLab 4.0.[50] The 10 lowest singlet excited states of the closed shell complexes were calculated within the time-dependent DFT (TD-DFT) formalism as implemented in Gaussian[51,52] in $CHCl_3$. The optimized molecular structures and the orbital isosurfaces were visualized using ArgusLab 4.0[50] whereas the Van der Waals surfaces were plotted employing Avogadro software.[53]

Supporting Information

Supporting Information is available from the Wiley Online Library or from the author.

Acknowledgements

This work was supported by National Natural Science Foundation of China (NSFC) (Grant No. 52002336) and Fundamental Research Funds for the Central Universities (SWU019041),

Chongqing Engineering Research Center for Rapid Diagnosis of Dread Disease and Chongqing Engineering Research Center for Micro-Nano Biomedical Materials and Devices, Southwest University, China (JL). This project has also received funding from the FWO and European Union's Horizon 2020 research and innovation programme under the Marie Skodowska-Curie grant agreement No.665501 (12U3417N LV) (FA).

Conflict of Interest

The authors declare no conflict of interest.

Keywords

lanthanide emission, dye sensitized nanoparticles, energy transfer, photosensitization, transient absorption spectroscopy

Received: ((will be filled in by the editorial staff))
Revised: ((will be filled in by the editorial staff))
Published online: ((will be filled in by the editorial staff))

References

[1] J.-C. G. Bünzli, C. Piguet, *Chem. Soc. Rev.* **2005**, *34*, 1048.

[2] J. Liu, A. M. Kaczmarek, R. Van Deun, *Chem. Soc. Rev.* **2018**, *47*, 7225.

[3] X. Chen, Y. Liu, D. Tu, *Lanthanide-doped luminescent nanomaterials*. Springer Science & Business Media, **2013**, ISBN 978-3-642-40364-4.

[4] Y. I. Park, H. M. Kim, J. H. Kim, K. C. Moon, B. Yoo, K. T. Lee, N. Lee, Y. Choi, W. Park, D. Ling, K. Na, W. K. Moon, S. H. Choi, H. S. Park, S.-Y. Yoon, Y. D. Suh, S. H. Lee, T. Hyeonet, *Adv. Mater.* **2012**, *24*, 5755.

[5] K. Liu, X. Liu, Q. Zeng, Y. Zhang, L. Tu, T. Liu, X. Kong, Y. Wang, F. Cao, S. A. G. Lambrechts, M. C. G. Aalders, H. Zhang, *ACS Nano* **2012**, *6*, 4054.

[6] Y. Liu, Y. Lu, X. Yang, X. Zheng, S. Wen, F. Wang, X. Vidal, J. Zhao, D. Liu, Z. Zhou, C. Ma, J. Zhou, J. A. Piper, P. Xi, D. Jin, *Nature* **2017**, *543*, 229.

[7] D. Tu, L. Liu, Q. Ju, Y. Liu, H. Zhu, R. Li, X. Chen, *Angew. Chem. Int. Ed.* **2011**, *50*, 6306.

[8] F. Wang, Y. Han, C. S. Lim, Y. Lu, J. Wang, J. Xu, H. Chen, C. Zhang, M. Hong, X. Liu, *Nature* **2010**, *463*, 1061.

[9] J. Liu, H. Rijckaert, M. Zeng, K. Haustraete, B. Laforce, L. Vincze, I. Van Driessche, A. M. Kaczmarek, R. Van Deun, *Adv. Funct. Mater.* **2018**, *24*, 1707365.

[10] K. A. White, D. A. Chengelis, K. A. Gogick, J. Stehman, N. L. Rosi, S. Petoud, *J. Am. Chem. Soc.* **2009**, *131*, 18069.

[11] S. Hao, Y. Shang, D. Li, H. Ågren, C. Yang, G. Chen, *Nanoscale* **2017**, *9*, 6711.

[12] B. Zhou, B. Shi, D. Jin, X. Liu, *Nat. Nanotech.* **2015**, *10*, 924.

[13] J. Zhou, D. Jin, *Nat. Photonics* **2018**, *12*, 378.

[14] L. Liang, X. Qin, K. Zheng and X. Liu, *Acc. Chem. Res.*, 2019, **52**, 228–236

[15] T. W. Schmidt, F. N. Castellano, *J. Phys. Chem. Lett.* **2014**, *5*, 4062.

[16] C. Du, H. Wang, F. Yang, P. C. Hammel, *Phys. Rev. B* **2014**, *90*, 140407(R).

[17] M. Seth, M. Dolg, P. Fulde, P. Schwerdtfeger, *J. Am. Chem. Soc.* **1995**, *117*, 6597.

[18] T. Förster, *Naturwissenschaften* **1946**, *33*, 166.

[19] S. Wen, J. Zhou, P. J. Schuck, Y. D. Suh, T. W. Schmidt, D. Jin, *Nat. Photonics* **2019**, *13*, 828.

[20] A. Beeby, S. Faulkner, D. Parker, J. A. G. Williams, *J. Chem. Soc., Perkin Trans. 2* **2001**, *8* 1268.

[21] G. L. Law, T. A. Pham, J. Xu, K. N. Raymond, *Angew. Chem. Int. Edit.* **2012**, *51*, 2371.

[22] D. J. Garfield, N. J. Borys, S. M. Hamed, N. A. Torquato, C. A. Tajon, B. Tian, B. Shevitski, E. S. Barnard, Y. D. Suh, S. Aloni, J. B. Neaton, E. M. Chan, B. E. Cohen, P. J. Schuck, *Nat. Photonics* **2018**, *12*, 402.

[23] C. M. G. Dos Santos, A. J. Harte, S. J. Quinn, T. Gunnlaugsson, *Coordin. Chem. Rev.* **2008**, *252*, 2512.

[24] B. Xue, D. Wang, L. Tu, D. Sun, P. Jing, Y. Chang, Y. Zhang, X. Liu, J. Zuo, J. Song, J. Qu, E. J. Meijer, H. Zhang, X. Kong, *J. Phys. Chem. Lett.* **2018**, *9*, 4625.

[25] R. Berera, R. Van Grondelle, J. T. M. Kennis, *Photosynth. Res.* **2009**, *101*, 105.

[26] T. Förster, Mechanisms of energy transfer. *Comprehensive Biochemistry*, Elsevier, New York, **1967**.

[27] J. Liu, A. M. Kaczmarek, F. Artizzu, R. Van Deun, *ACS Photonics* **2019**, *6*, 659.

[28] X. P. Chen, W. J. Zhang, Q. Y. Zhang, *Physica B* **2011**, *406*, 1248.

[29] W. Zou, C. Visser, J. A. Maduro, M. S. Pshenichnikov, J. C. Hummelen, *Nat. Photonics* **2012**, *6*, 560.

[30] F. Quochi, M. Saba, F. Artizzu, M. L. Mercuri, P. Deplano, A. Mura, G. Bongiovanni, *J. Phys. Chem. Lett.* **2010**, *1*, 273.

[31] F. Artizzu, F. Quochi, L. Marchiò, C. Figus, D. Loche, M. Atzori, V. Sarritzu, A. M. Kaczmarek, R. Van Deun, M. Saba, A. Serpe, A. Mura, M. L. Mercuri, G. Bongiovanni, P. Deplano, *Chem. Mater.*, **2015**, *27*, 4082.

[32] G. K. Mor, J. Basham, M. Paulose, S. Kim, O. K. Varghese, A. Vaish, S. Yoriya, C. A. Grimes, *Nano Lett.* **2010**, *10*, 2387.

[33] W. Wei, G. Chen, A. Baev, G. S. He, W. Shao, J. Damasco, P. N. Prasad, *J. Am. Chem. Soc.* **2016**, *138*, 15130.

[34] P. Geiregat, A. J. Houtepen, L. K. Sagar, I. Infante, F. Zapata, V. Grigel, G. Allan, C. Delerue, D. Van Thourhout, Z. Hens, *Nat. Mater.* **2018**, *17*, 35.

[35] A. Sciortino, M. Gazzetto, M. L. Soriano, M. Cannas, S. Cárdenas, A. Cannizzo, F. Messina, *Phys. Chem. Chem. Phys.* **2019**, 21, 16459.

[36] M. W. Mara, D. S. Tatum, A.-M. March, G. Doumy, E. G. Moore, K. N. Raymond, *J. Am. Chem. Soc.* **2019**, *141*, 11071.

[37] P. Geiregat, J. Maes, K. Chen, E. Drijvers, J. De Roo, J. M. Hodgkiss, Z. Hens, *ACS Nano* **2018**, *12*, 10178.

[38] T. Förster, *Discuss. Faraday Soc.* **1959**, *27*, 7.

[39] R. Deng, J. Wang, R. Chen, W. Huang, X. Liu, *J. Am. Chem. Soc.* **2016**, *138*, 15972.

[40] M. Kuss-Petermann, O. S. Wenger, *J. Am. Chem. Soc.* **2016**, *138*, 1349.

[41] J. Zhang, H. J. Kulik, T. J. Martinez, J. P. Klinman, *P. Natl. Acad. Sci. USA* **2015**, *112*, 7954.

[42] D. L. Dexter, *J. Chem. Phys.*, **1953**, *21*, 836.

[43] H. Dong, L. Sun, L. Li, R. Si, R. Liu, C. Yan, *J. Am. Chem. Soc*. **2017**, *139*, 18492.

[44] R. G. Parr, W. Yang, Density functional theory of atoms and molecules, **1989**, Oxford University Press, Oxford.

[45] M. J. Frisch et al., Gaussian 16 Revision C.01, **2016**, Gaussian, Inc., Wallingford CT.

[46] D. Becke, *J. Chem. Phys.* **1993**, *98*, 5648.

[47] C. Lee, W. Yang, R. G. Parr, *Phys. Rev. B* **1988**, *37*, 785.

[48] R. Krishnan, J. S. Binkley, R. Seeger, J. A. Pople, *J. Chem. Phys.* **1980**, *72*, 650.

[49] A. D. McLean, G. S. Chandler, *J. Chem. Phys.* **1980**, *72*, 5639.

[50] M. A. Thompson, ArgusLab 4.0.1, Planaria Software LLC: Seattle, WA, **2004**. Available at: http://www.arguslab.com/arguslab.com/ArgusLab.html/.

[51] V. Barone, M. Cossi, *J. Phys. Chem. A* **1998**, *102*, 1995.

[52] M. Cossi, N. Rega, G. Scalmani, V. Barone, *J. Comp. Chem.* **2003**, *24*, 669

[53] Avogadro: an open-source molecular builder and visualization tool. Version 1.0.1, http://avogadro.cc/.

A hereto hidden energy transfer pathway occurring via dye singlet states in lanthanide doped nanoparticles has been revealed. It is demonstrated that energy transfer is strictly regulated by a distance-dependent regime, where sub-0.5 nm sized dye molecules are key to realize fully efficient photosensitization.

Jing Liu, Pieter Geiregat, Luca Pilia, Rik Van Deun and Flavia Artizzu*

Molecular size matters: ultrafast dye singlet sensitization pathways to bright nanoparticle emission